

Tracer transport in a fractured chalk: X-ray CT characterization and digital-image-based (DIB) simulation

W. C. Zhu · J. Liu · D. Elsworth · A. Polak ·
A. Grader · J. C. Sheng · J. X. Liu

Received: 5 April 2005 / Accepted: 15 November 2006 / Published online: 25 January 2007
© Springer Science+Business Media B.V. 2006

Abstract A digital-image-based simulation methodology is applied to evaluate the influence of heterogeneous porosity on the evolution of tracer concentrations in imaged tracer tests. Maps of computed tomography (CT)-number are calibrated relative to average porosity, and then thresholded to define porosity maps. These data are then used to automate the distribution of parameters within a finite element representation of the geometry. The technique is applied to characterize the variability of the porosity, the hydraulic conductivity, and the diffusivity for an artificially fractured chalk core (30 × 5 cm). X-ray CT was used both to characterize the initial condition of the core, and then to concurrently monitor the transport of an NaI tracer within the fracture and into the surrounding matrix. The X-ray CT imaging is used to characterize the heterogeneous rock porosity, based on which the hydraulic conductivity, and diffusivity of the chalk were defined and were directly imported into our newly developed three-dimensional FEMLAB-based multiple physics simulator. Numerical simulations have confirmed the observed tracer transport behaviors: (1) The different tracer-penetration distances imaged in the matrix above and below the horizontal fracture are indicative of a greater tracer mass penetrating into the lower matrix; and (2) Transport in the matrix below the fracture was enhanced. The computer simulated tracer concentration distributions compare favorably with those monitored by X-ray CT.

W. C. Zhu · J. Liu (✉) · J. C. Sheng · J. X. Liu
School of Oil and Gas Engineering, The University of Western Australia, WA, 6009, Crawley,
Australia
E-mail: jishan@cyllene.uwa.edu.au

D. Elsworth · A. Grader
Department of Energy and Geo-Environmental Engineering, Penn State University,
University Park, USA

A. Polak
Department of Civil and Environmental Engineering, Technion, Israel Institute of Technology,
Haifa 32000, Israel

Keywords Tracer diffusion · Rock heterogeneity · Porosity · DIB simulation · Imaging

List of symbols

C	Concentration in terms of mass fraction (dimensionless)
D	Diffusion coefficient (m^2/s)
$f_k(i, j)$	Discrete function to express the digital image in RGB color space, where $k = 1, 2,$ and 3 (dimensionless)
\mathbf{g}	Gravity acceleration (vector) (m/s^2)
H, S, I	Hue, saturation and intensity for HSI color space of the digital image (dimensionless)
k	Permeability (m^2)
M, N	Number of pixels in horizontal and vertical directions for a digital image (dimensionless)
P	Fluid pressure (Pa)
R, G, B	Red, green, and blue components for RGB color space of digital image (dimensionless)
S_s	The specific storativity of the porous medium ($1/\text{m}$)
t	Time (s)
$\mathbf{u}^l(u_i^l)$	Pore velocity vector of fluid (m/s)
ϕ	Porosity (dimensionless)
μ_l	Liquid dynamic viscosity ($\text{Pa}\cdot\text{s}$)
ρ_l	Liquid density (kg/m^3)

1 Introduction

Rock comprises multiple components including mineral grains and cements, separated by interstitial voids manifest as pores and cracks. Each component may exhibit different flow and transport properties—contributing to the relative dominance of diffusive or reactive fluxes. The realistic characterization of this heterogeneity has been a long-standing problem of great practical interest, especially in petroleum reservoir engineering (Santos et al. 2002; Qi et al. 2000) because it may significantly affect productivity. Both multiphase flow and solute transport in subsurface fractured rock are highly sensitive to hydraulic anisotropy and heterogeneity. Local permeability contrasts may promote ‘channelized’ flow and also create local reservoirs for solutes. Combined, these features may result in rapid initial breakthroughs that are both broadly distributed in space, and of extended duration (long-tailed) in decay. These features importantly impact the fidelity of performance predictions for critical facilities such as repositories for high-level radioactive wastes. Since fractures and matrix may exhibit order-of-magnitude differences in permeabilities, porosities, and reactivities, it is extremely difficult to design measurement devices and monitoring systems that capture these multiple attributes simultaneously (Finsterle et al. 2002). These are only two typical examples for a host of contemporary engineering phenomena. The primary objective of this work is to illustrate the dependence of convective-diffusive transport on local heterogeneity where this heterogeneity is characterized

and quantified by an integrated investigation by X-ray computed tomography (CT). The principal features of the spatial heterogeneity are accommodated through digital-image-based finite element simulation.

1.1 Statement of the problem

The classic convection-diffusion equation is defined as

$$\frac{\partial}{\partial t}(\phi C) + \nabla \cdot (-\phi D \cdot \nabla C + C \cdot \mathbf{u}^l) = 0, \quad (1)$$

where C is the concentration in terms of mass fraction, ϕ is the porosity, D is diffusion coefficient, and \mathbf{u}^l is the Darcy velocity. Traditionally, ϕ is treated as a constant and Eq. 1 is re-written as

$$\frac{\partial C}{\partial t} + \nabla \cdot \left(-D \cdot \nabla C + C \frac{\mathbf{u}^l}{\phi} \right) = 0. \quad (2)$$

This simplification is not readily justified when studying diffusive-convective process in fractured rocks. A rock mass is a fractured porous medium containing pre-existing fractures of various dimensions, under complex in situ conditions of stress, temperature, and fluid pressures. Furthermore, intact rock consists of many individual materials and components, representing a variety of length scales, including mineral grains, cements, and voids of various geometries. Each component may have different flow and transport properties. Their complex combination of constituents, and the long and often complex history of formation, makes porosity a space-dependent variable. The impact of space-dependent porosity, $\phi(x, y, z)$, on the diffusive-convective process in fractured rock is the specific motivation of this study.

1.2 Quantitative imaging

To fully understand the impact of heterogeneity, it is becoming increasingly clear that the accurate characterization of actual micro-scale features of rock and their direct incorporation into flow simulations are needed. Recent applications of X-ray CT techniques (Polak et al. 2003; Wildenschild et al. 2002) have made it possible to achieve this goal. The usefulness of this technique in geological and geotechnical research has been demonstrated by many studies. The X-ray CT technique has been applied to measure fracture geometry (Montemagno and Pyrak-Nolte 1999); to investigate tracer diffusion from fractures into the surrounding rock matrix (Polak et al. 2003; Tidwell et al. 2000; Nakashima 2000); to conduct analyses of geological processes such as the texture of igneous and metamorphic rocks (Karacan and Mitchell 2003); to characterize and determine distributions of saturation and porosity (Withjack and Durham 2001; Schembre and Kovscek 2003); to determine contact areas in rock joints (Scavia 1999); to characterize gas adsorption and transport in coal seams (Karacan and Mitchell 2003) and to determine foam-induced fluid partitioning in porous media (Nguyen et al. 2003, 2005; Zitha et al. 2003). In recent applications the X-ray CT technique has been used to visualize in situ fluid flow within deformed rock during permeability testing under atmospheric pressure (Hirono et al. 2003). These applications demonstrate the utility of X-ray CT in the characterization of both geologic media and processes.

1.3 Digital-image-based simulation

Detailed quantitative maps of spatially variable physical properties are required for any numerical models that solve the governing equations of fluid flow and transport in rocks. In previous studies, the inhomogeneities and microstructures of rock materials have been simulated via statistical tools or random distribution packages (Tang 1997; Blair and Cook 1998; Tang et al. 2000; Zhu and Tang 2004). The salient feature of these statistical models is that rock heterogeneity is described by assigning different material properties to the microstructures (such as fractures) for which no additional constitutive laws are separately specified. However, the question then arises of how statistical distributions relate to the fields in one realization of the rock. For fractured rock, it is not always reasonable to neglect the existence of local heterogeneity and to assume it to be a uniform heterogeneous material. By their nature, the localization of mechanical, hydrological or diffusive characteristics near the fractures would not be captured and their effects would not be quantified by using these statistical models. Therefore, artificial realizations of internal heterogeneities or microstructures based on statistical or random distributions are incapable of representing the actual local geometrical and constitutive variations of microstructures in rocks. This inability may prevent us from understanding the real impact of the local heterogeneity on flow and transport processes in rocks.

Some recent studies have shown that digitalized image data, such as the characteristics of different minerals and fractures, can be used to establish the heterogeneity of rock. Digital image processing (DIP) has been widely used in medical diagnosis, the design of material composites (Takano et al. 2003; Chermant 2001). More recently, DIP has been used in rock mechanics to detect the geometry of discontinuities in rock masses (Santos et al. 2002; Hadjigeorgiou et al. 2003; Daian et al. 2004) or to analyze the failure process and cracking behavior of rock (Tham et al. 2003). These applications have included extension to digital-image-based numerical modeling that accommodates initial distributions of minerals within rock (Yue et al. 2003; Chen et al. 2004).

1.4 About this study

Through this study, the digital-image-based simulation technique is extended to quantify the impact of local heterogeneity in porosity on diffusion-convection in a fractured chalk. The spatial distributions of both porosity (porosity map) and tracer concentration (concentration map) are obtained from X-ray CT scans. The porosity map is then directly incorporated into a three-dimensional (3D) FEMLAB-based computer simulator. The validity of the computer simulator is verified through comparing the simulated tracer concentration maps with those recovered from the core by X-ray CT.

2 X-ray CT characterization

Results are reported for a tracer diffusion experiment conducted within an artificial longitudinal fracture within a cylindrical core of chalk. Convective transport and diffusion of a 5% NaI tracer into the chalk matrix was monitored using a second-generation X-ray CT scanner. Experimental results are reported in a companion paper (Polak



Fig. 1 Schematic representation of the fractured core used in X-Ray CT experiments

et al. 2003). For completeness, the experimental description and relevant results are summarized in the following sections.

2.1 Experimental description

2.1.1 Rock sample

The chalk sample used in the experimental study was retrieved at a depth of ~ 86 m from a borehole located in the northern Negev desert, Israel. A detailed description of the study area can be found in Nativ et al. (1999). Laboratory measured porosity and permeability magnitudes are 41% and 1.04 mD, respectively. The mineralogy of the chalk sample consisted mainly of calcite (90%) with insoluble residue (8.1%) containing quartz, opal-CT, clinoptilolite, and some clay. The core sample was fractured using a Brazilian-like test (Vukuturi et al. 1974). A longitudinal plane fracture was obtained by compressing the cylindrical sample between two opposite plates, thereby inducing tensile stress at its center. A 10-cm-long, 5-cm diameter core piece was used for the experiment, containing a fracture that started at the core's center at one end, and dipped toward the other end (Fig. 1). Although the core was artificially fractured (and consequently, the fracture walls were unaffected by weathering, effects of historic transport, etc.), the major characteristics of the diffusion process into, within, and out of the matrix could be properly evaluated.

The artificially fractured core was placed in a CT scanner after it was water saturated, then a tracer solution was injected into the horizontal fracture. The concentration distribution within the upper and lower parts of the core (above and below the fracture, respectively) was monitored in time using consecutive CT scans.

2.1.2 Experimental setup

The experimental apparatus included a CT scanner, a core holder, and a fluid-injection system (Fig. 2). The CT system used to monitor the solute concentrations during the experiment was a second-generation medical-based X-ray CT scanner (Deltascan 100). The scanner produces two-dimensional slices through the sample with a thickness of 8 mm and an in-plane pixel resolution of about 0.4 mm. The X-ray energy level used in the experiment was 120 kV at 25 mA, and the acquisition time for each

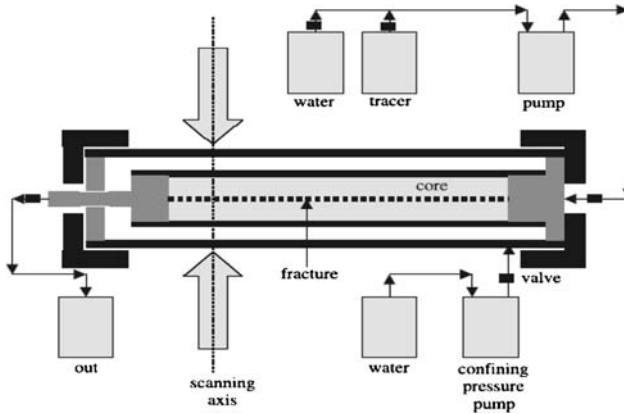


Fig. 2 Schematic description of the experimental setup for X-Ray CT scans

scan was 2 min. Two positioning tables were mounted on either side of the CT system to which the sample-holder assembly was connected. These positioning tables enabled back-and-forth movement of the sample holder during the scanning process. The sample and the holder were placed in the scanner at the beginning of the experiment and not removed during the experiment, ensuring proper registration of the CT images. The core holder contained holes to allow fluids to enter and exit the core. A liquid chromatography pump was used to inject water or solution into the fracture intersecting the core sample. The outlet side of the core enabled external measurement of the injection flow rates (Fig. 2).

2.1.3 Experimental procedure

Prior to closing the two halves of the core sample, small pieces of crushed chalk were placed at a few points along the fracture to keep it open. The core was then inserted into a rubber sleeve and placed inside the core holder. Water was then pumped into the space between the rubber sleeve and the core-holder walls to create confining pressure (0.5 MPa, to keep the core sample in place and minimize fluid bypass along its outer edges). Following core-packing, the first scan was carried out (dry calibration) to determine whether the fracture was completely open throughout its length. Scanning was performed in 0.42-cm steps, resulting in 22 images (slices) covering the entire length of the core in each scanning sequence. This scanning procedure was carried out throughout the rest of the experiment. Following the first scan, the core was put under a vacuum of 500 AHg for 24 h. Distilled water was then injected into the core, while closing the vacuum pump, and saturation of the core began. Complete saturation was obtained after 12 h during which a number of confirmatory scans were taken. The first scan run on the fully saturated core served as a reference for the subsequent tracer-solution injection.

Following core saturation, the tracer solution (5% by weight of NaI) was injected into the horizontal fracture at a constant concentration and rate of $2.5 \text{ cm}^3/\text{min}$ (Fig. 2). The volume of the fracture void was about 5 cm^3 ; hence, the solution was replaced every 2 min. This injection process lasted for 7 days, during which the core was scanned

nine times (hereafter, denoted as sequences 1 through 9) to track the tracer invasion into the chalk matrix above and below the fracture.

2.2 Experimental results

2.2.1 Porosity map

The average porosity of the entire core was calculated using the net amount of water injected into the core during the saturating phase and was found to be 39.2%. This value represents the net volume of water penetrating into the matrix and excludes “dead volumes” stored in the fracture void or in the solution-feeding tubes. The porosity distribution of each image (of the 22 scanned) was calculated using the CT analysis presented by Vinegar and Wellington (1987). The net water (converted to an internationally standardized scale, known as Hounsfield units (HU), usually expressed as $HU = 1,000(\nu - \nu_W)/\nu_W$, where ν_W is the linear attenuation coefficient of water [cm^{-1}]). The scale is linear, and HU units for air and water are defined as $-1,000$ and 0 , respectively. High HU numbers correspond to high-density materials, for each pixel in each image was determined by the difference between the wet and dry scans. A factor, specific for the scanned chalk core, was calculated by dividing the average porosity (39.2%) by the average CT number determined for all 22 images. The porosity in each pixel was then determined by multiplying the net water specific to this pixel (in HU units) by that factor. Figure 3 shows a typical porosity distribution of image 1, which is located 5 cm downstream from the inlet, as calculated by this method. The red color represents the fracture because of its high porosity values. The rest of the matrix shows an almost homogeneous porosity distribution, which implies lack of lithological variations. Five rectangular shapes, each covering an area of 3.8×23 mm (10×60 pixels), are also shown in Fig. 3. The average porosity of each rectangle is shown and was calculated by the method described above. The porosity of the rectangle containing the fracture is not 100% (as expected) because the fracture does not consist of two parallel plates separated by an empty void. Instead, the fracture void is spatially variable and contains asperities and spacers to keep the fracture from closing when confining pressure is applied. The porosity in the rock matrix is not constant and uniformly distributed, but is spatially heterogeneous.

2.2.2 Concentration maps

To assess the concentration of tracer that in the matrix above and below the fracture, the following method was carried out: at each pixel. The CT number registered during the wet scan was subtracted from those registered during each of the nine diffusion scans to obtain the net tracer CT number of that pixel for that individual diffusion scan. By adding this number, characterizing a single pixel, to the numbers characterizing other neighboring pixels (consisting of a desired grid) during an individual diffusion scan, the cumulative tracer contained in that area was obtained. The distribution of tracer concentration away from the fracture is shown qualitatively at different times in Fig. 4a through c. In the first scanning sequence (taken about 1 h following the beginning of tracer injection) the tracer had not completely filled the fracture void and the surrounding matrix. During the subsequent scans, the tracer concentration remained constant within the fracture, but penetration into the lower core-half was more rapid than in the upper half. Polak et al. (2003) proposed a 1D

model to simulate tracer transport in the rock matrix, and to calibrate for diffusion coefficients. Calibrated magnitudes for diffusion coefficients for the upper and lower halves of the rock sample are defined as 7.0×10^{-10} and 9.5×10^{-10} m²/s, respectively.

3 3D DIB Simulations

In this section, a 3D digital-image-based (DIB) model is developed to represent these experimental observations. The 3D model is built from the image shown in Fig. 3. Using maps of porosity as a direct input, and specification of hydraulic conductivity, and diffusion coefficient based on porosity map as indirect inputs, the model was used to predict the maps of tracer concentration. These input maps characterize the heterogeneities of porosity, hydraulic conductivity and diffusion coefficient in both the rock matrix and the fracture. The distribution of porosity, hydraulic conductivity and diffusion coefficient defined at this cross section is extrapolated to the whole length of the rock core. The predicted concentration maps were compared with the CT monitored ones.

Fig. 3 Porosity distribution in a cross-section (5 cm from the inlet side) of the rock sample, determined through CT scanning

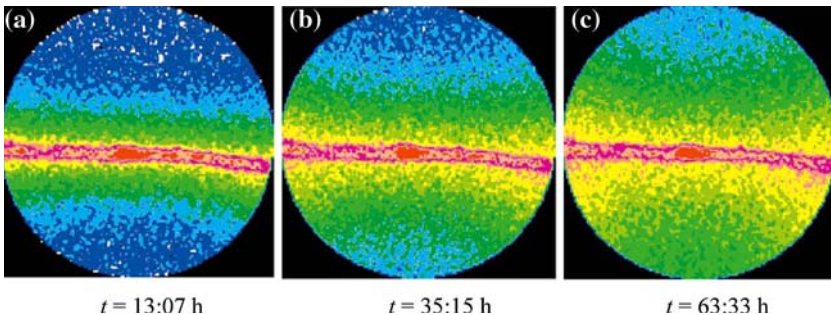
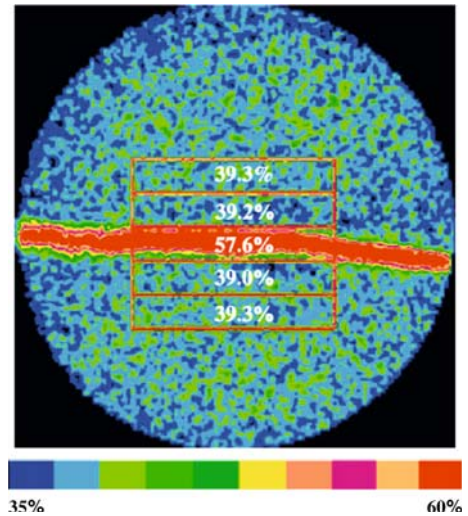


Fig. 4 Tracer concentration maps determined through CT scanning for the cross-section 5 cm downstream from the inlet

3.1 Governing equations

3.1.1 Flow equation

The governing equation for saturated fluid flow in porous medium is described by a liquid mass balance equation,

$$S_s \frac{\partial P}{\partial t} - \nabla \cdot \left[\frac{k \rho_l \mathbf{g}}{\mu_l} \cdot (\nabla P - \rho_l \mathbf{g}) \right] = 0, \quad (3)$$

where P is the pore fluid pressure within the porous continuum (Pa), S_s is the specific storage of the porous medium (1/m), ρ_l the liquid density (kg/m^3), μ_l is the liquid dynamic viscosity (Pa·s), t the time (seconds), k the permeability (m^2), and \mathbf{g} is the gravitational acceleration (vector) (m/s^2).

3.1.2 Transport equation

The transport of mass by simultaneous diffusion and convection is described by the following parabolic partial differential equation as given in Eq. 1, in which the time-dependent Darcy velocity \mathbf{u}^l is calculated as:

$$\mathbf{u}^l = -\frac{k}{\mu_l} \cdot (\nabla P - \rho_l \mathbf{g}), \quad (4)$$

where k is also permeability (m^2) and P is pore fluid pressure (Pa) that is evaluated from Eq. 3.

To solve the above coupled governing equations, the following boundary conditions and initial conditions for the saturated porous medium are considered:

$$P(\mathbf{x}, t) = \bar{P}(\mathbf{x}, t) \quad t \in [0, \infty), \quad (5)$$

$$-\frac{\mathbf{k}}{\mu_l} \cdot (\nabla P - \rho_l \mathbf{g}) \cdot \mathbf{n}(\mathbf{x}) = \bar{Q}_l(\mathbf{x}, t) \quad t \in [0, \infty), \quad (6)$$

$$C(\mathbf{x}, t) = \bar{C}(\mathbf{x}, t) \quad t \in [0, \infty), \quad (7)$$

$$(-D \cdot \nabla C + \mathbf{u} \cdot C) \cdot \mathbf{n}(\mathbf{x}) = \bar{I}_C(\mathbf{x}, t) \quad t \in [0, \infty), \quad (8)$$

$$(-D \cdot \nabla C) \cdot \mathbf{n}(\mathbf{x}) = \mathbf{0} \quad t \in [0, \infty), \quad (9)$$

$$P(\mathbf{x}, 0) = P_0 \quad \text{on } V, \quad (10)$$

$$C(\mathbf{x}, 0) = C_0 \quad \text{on } V, \quad (11)$$

where \mathbf{x} is the coordinates, quantity V represents the volume under consideration, and \bar{P} , \bar{Q}_l , \bar{C} , and \bar{I}_C represent known fluid pressure, flow flux, tracer concentration and diffusion mass flux at the boundaries, respectively. In order to solve Eqs. 1, 3 through 11, three parameters of, porosity, hydraulic conductivity, and diffusion coefficient need to be specified. In this study, these parameters were directly or indirectly determined based on the X-ray CT images using image processing techniques.

3.2 Digital image processing technique

Sectional images of the core are obtained via X-ray CT scanning. For this kind of RGB image, at each pixel there are three integer values to represent the red, green,

and blue, so the color image data consist of three discrete functions, $f_k(i, j)$, where $k = 1, 2, \text{ or } 3$, in the i and j Cartesian coordinate system:

$$f_k(i, j) = \begin{bmatrix} f(1, 1) & f(1, 2) & \cdots & f(1, M) \\ f(2, 1) & f(2, 2) & \cdots & f(2, M) \\ \vdots & \vdots & \ddots & \vdots \\ f(N, 1) & f(N, 2) & \cdots & f(N, M) \end{bmatrix} \quad (k = 1, 2, \text{ and } 3), \quad (12)$$

where i varies from 1 to N , and j from 1 to M . M and N are the number of pixels in the horizontal and vertical directions, respectively.

In this work we use MATLAB to read the image file in JPEG format to obtain the discrete function, $f_k(i, j)$. As an alternative to the RGB color space, the HSI color space may be substituted, as it is close to how humans perceive colors. HSI is an acronym for hue, saturation, and intensity. The hue component (H) represents repression related to the dominant wavelength of the color stimulus. Therefore, the hue is the domain color perceived by human beings. The saturation component (S) signals how much the color is polluted with white color. The intensity component (I) stands for brightness or lightness and is irrelevant to colors. In general, hue, saturation, and intensity are obtained by different transformation formulae through converting numerical values of R , G , and B in the RGB color space to the HSI color space (Gonzalez and Woods 1992).

Distinct microstructures (such as fractures and minerals) in the rock sample are acquired according to the values of H , S , or I of individual pixels, and the different material properties (such as permeability) are specified for each pixel. If the material properties of different minerals or structures are known in advance, by this means, the relation between values of H (S , or I) of the digital image and its materials properties can be uniquely established.

Figure 5 presents the distribution of the values of H , which are calculated based on the digital RGB image of the porosity map (as shown in Fig. 3). Correspondingly, the values of H along the vertical cross-section of the core sample are also plotted. For the H graph, which describes a pure color, the distinction between the fracture and the rock matrix can be clearly made because the H -values of the fracture are much lower than those of the rock matrix. This technique can also be extended to 3D conditions if the 3D image of the rock microstructures are available or the 3D microstructures can be reconstructed based on a series of 2D cross-sectional images.

Figure 6 presents different characterizations of the fracture obtained from the DIP technique when three different thresholds of H -values are selected to distinguish the fracture and rock matrix. When the thresholds of H -values are specified to be 0.12 or 0.08, a relative wide and open fracture is captured (as shown in Fig. 6a, b). Apparently, this is not the case because the fracture is not fully open. By contrast, when the threshold of the H -value is specified to be 0.04, as shown in Fig. 6c, the fracture is not totally open, but partly filled with rock fragments, which is phenomenally consistent with the rock sample, and it is adopted in this study.

3.3 Finite element analysis

The complete set of coupled Eqs. 1, 3 through 11 is implemented into, and solved by using FEMLAB, a powerful PDE-based multiphysics modeling environment. For the experiment as discussed in Sect. 2.1, tracer diffusion evolved predominantly in

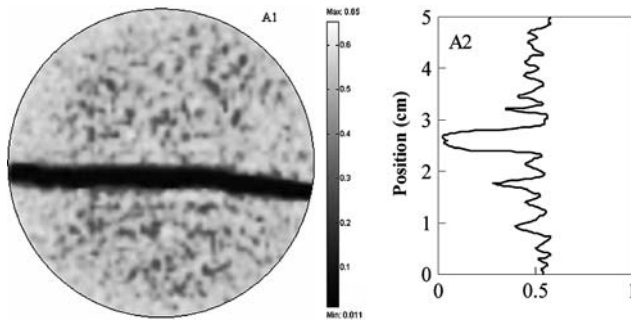


Fig. 5 Distributions of H -values obtained from DIP technique, where A1 represents the H distribution maps and A2 represents the H distribution profiles along the vertical diameter

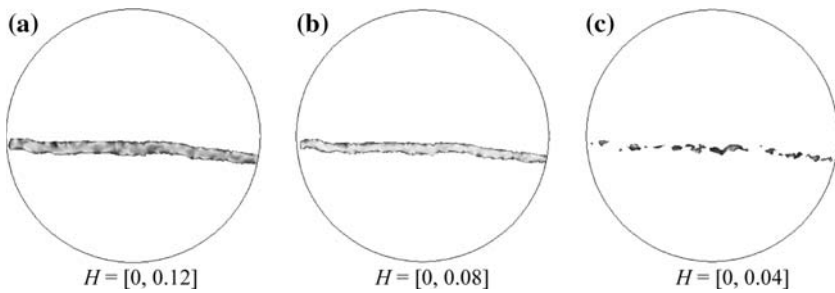


Fig. 6 Fractured zone under different thresholds of H -values

the direction perpendicular to the flow, therefore a 3D numerical analysis is necessary. In our simulations, the rock core, which is 5 cm in diameter and 10 cm in length, is discretized into 208,034 tetrahedral finite elements. The boundary conditions are specified as shown in Fig. 7. The external boundary, excepting inlet, and outlet ends of the cylindrical core sample, are no-flow and no-diffusion boundaries. For the fluid flow analysis, a hydraulic pressure of 1.0 kPa is applied at the inlet side and zero hydraulic pressure is specified at the outlet side of the core sample. For the transport analysis, a relative concentration of unity is specified at the inlet side, while the convective flux is specified to the outlet side of the core sample. In the domain including the fracture and rock matrix, the fluid flow and convection-diffusion process are defined by Eqs. 3, 1, respectively.

The permeability and diffusion of rock matrix cannot be determined directly based on X-ray CT scanning, but can be estimated based on their relations with the porosity that is obtained from X-Ray CT scanning. For example, it is possible to convert porosity map into permeability map by the conventional Carman–Kozeny relationship (Kozeny 1927; Carman 1938), depending on tortuosity and particle size differences; similarly the diffusion coefficient is also related to porosity and tortuosity in sediments (Nakashima 1995). Here, as used by other researchers (Koh et al. 1996; Diabira et al. 2001), in the rock matrix we assume one of the simplest forms of porosity–permeability relationship

$$k(x, y, z) = k_0 \left[\frac{\phi(x, y, z)}{\phi_0} \right]^\gamma, \tag{13}$$

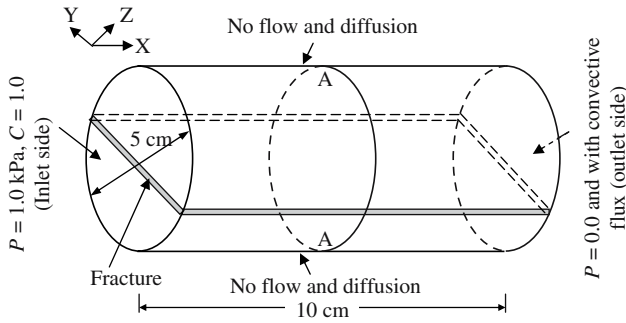


Fig. 7 The boundary conditions for the simulation model, where the tracer is injected at left, and flows out at right. The cross section A–A is located 5 cm downstream from the inlet, and is used for the representation of simulation results

where k_0 and ϕ_0 are overall apparent permeability and porosity of the rock specimen, respectively. And $k(x, y, z)$ and $\phi(x, y, z)$ are permeability and porosity at the position whose coordinate is (x, y, z) . γ is the porosity–permeability factor, which is in the range of 6–9 for diatomite (Koh et al. 1996). In this study, γ is specified to be 6.0.

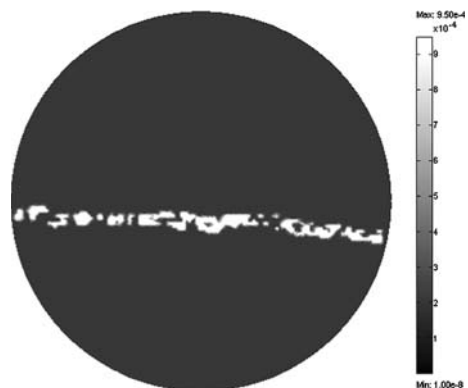
Similarly, the diffusivity–porosity relationship in the rock matrix is expressed as

$$D(x, y, z) = D_0 \left[\frac{\phi(x, y, z)}{\phi_0} \right]^\xi, \tag{14}$$

where D_0 is overall diffusion coefficient, and $D(x, y, z)$ and $\phi(x, y, z)$ are diffusion coefficient and porosity at the position whose coordinate is (x, y, z) , respectively; ξ is porosity–diffusivity factor. Based on other studies (Koh et al. 1996; Diabira et al. 2001), $\xi = 3.0$ is adopted for this study.

The permeability in the fracture is unknown and is determined through using the flow rate as a constraint. The underlying principle is that the simulated flow rate remains the same as the value in the experiment ($2.5 \text{ cm}^3/\text{min}$). This is achieved by choosing different values of its permeability. At last, a permeability of $1.4 \times 10^{-10} \text{ m}^2$ is determined for the fracture. The spatial distribution of the permeability in this fractured rock is mapped as shown in Fig. 8.

Fig. 8 The distribution of hydraulic conductivity in the cross section, that is, 5 cm downstream from the inlet. Color bar shows the magnitude of hydraulic conductivity in the unit of m/s



The remaining parameter for the simulation is the overall diffusion coefficient representative of the rock matrix (D_0). Previously (Polak et al. 2003), a 1D model was used to determine the magnitude of the diffusion coefficient representative of the rock matrix. By using that technique, the magnitude was determined as $7.0 \times 10^{-10} \text{ m}^2/\text{s}$. The diffusion coefficient of the fracture is assumed to be 1,000 times that of rock matrix, corresponding to the product of advective velocity and coefficient of longitudinal dispersion estimated as one-tenth of the sample length. This diffusion coefficient is used to indicate the molecular diffusion that is the most straightforward spreading mechanism to discern as it is independent of fluid velocity. The other relevant parameters used in the finite element analysis are listed in Table 1.

3.4 Numerical results

The simulated distributions of the tracer concentration at the vertical cross section A–A (5 cm downstream from the inlet) are shown in Fig. 9 for variable magnitudes of the diffusion coefficient between 2.0×10^{-10} and $7.0 \times 10^{-10} \text{ m}^2/\text{s}$.

Table 1 Other related parameters used in the numerical analysis

Parameters	Value
Porosity, ϕ (dimensionless)	Specified according to Fig. 3 based on DIB technique
Specific storativity, S_s (1/m)	0.0
Density of fluid, ρ_l (kg/m ³)	1.0×10^3
Liquid dynamic viscosity, μ_l (Pa·s)	1.0×10^{-3}
Gravity acceleration, g (m/s ²)	9.8 m/s^2

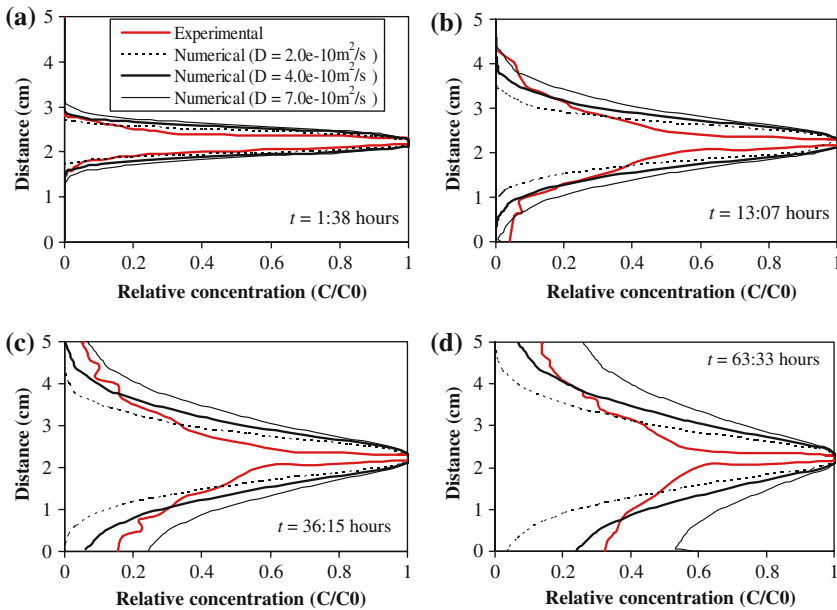


Fig. 9 Simulated distributions of the tracer concentration along the vertical diameter of cross section A–A for different diffusion coefficients

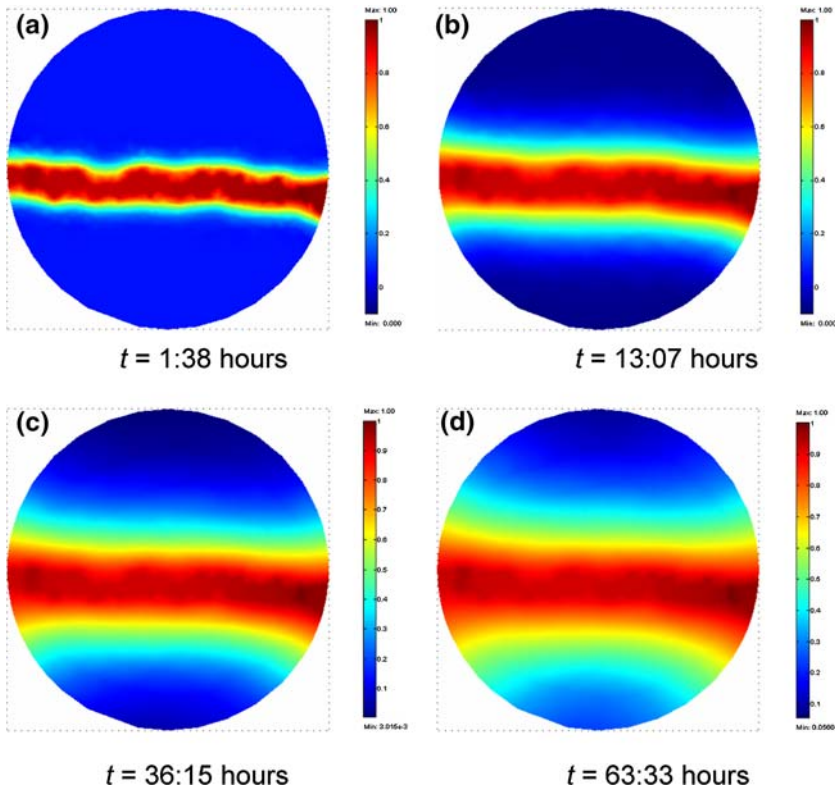


Fig. 10 Simulated distributions of the tracer concentration at cross section A–A at sequential times, where the diffusion coefficient of the rock matrix is equal to $4.0 \times 10^{-10} \text{ m}^2/\text{s}$, and the *color bar* indicates the relative magnitude of tracer concentration

The selected magnitude of $7.0 \times 10^{-10} \text{ m}^2/\text{s}$ overestimates the role of diffusion, relative to convection. This has been confirmed by model results: the predicted tracer concentration is larger than the experimental one when the estimated diffusion coefficient (i.e., $7.0 \times 10^{-10} \text{ m}^2/\text{s}$) was used in the 3D model. Through comparisons, best matches between simulated concentrations and experimental ones were achieved when the diffusion coefficient is equal to $4.0 \times 10^{-10} \text{ m}^2/\text{s}$. In this study, we treat the porosity as a function of space. This may explain why the best-fit average diffusion coefficient ($4.0 \times 10^{-10} \text{ m}^2/\text{s}$) is smaller than the 1D model result ($7.0 \times 10^{-10} \text{ m}^2/\text{s}$).

In the following analyses, we assume a diffusion coefficient of $4.0 \times 10^{-10} \text{ m}^2/\text{s}$ as the most likely magnitude for the rock sample. Distributions of the tracer concentration and the convective flux at cross section A–A are shown in Fig. 10. It is apparent that the tracer concentration in the fracture reaches 1.0 early within the experiment ($t = 1:38 \text{ h}$). This is because the high-velocity flow enhances tracer convection within the fracture. Throughout the following time steps, the tracer concentration remains constant (it is 1.0) within the fracture, and progressively diffuses into rock matrix above and below the fracture.

Three-dimensional distributions of the tracer concentration are shown in Fig. 11. Due to boundary effects, the tracer concentration along the length of core sample

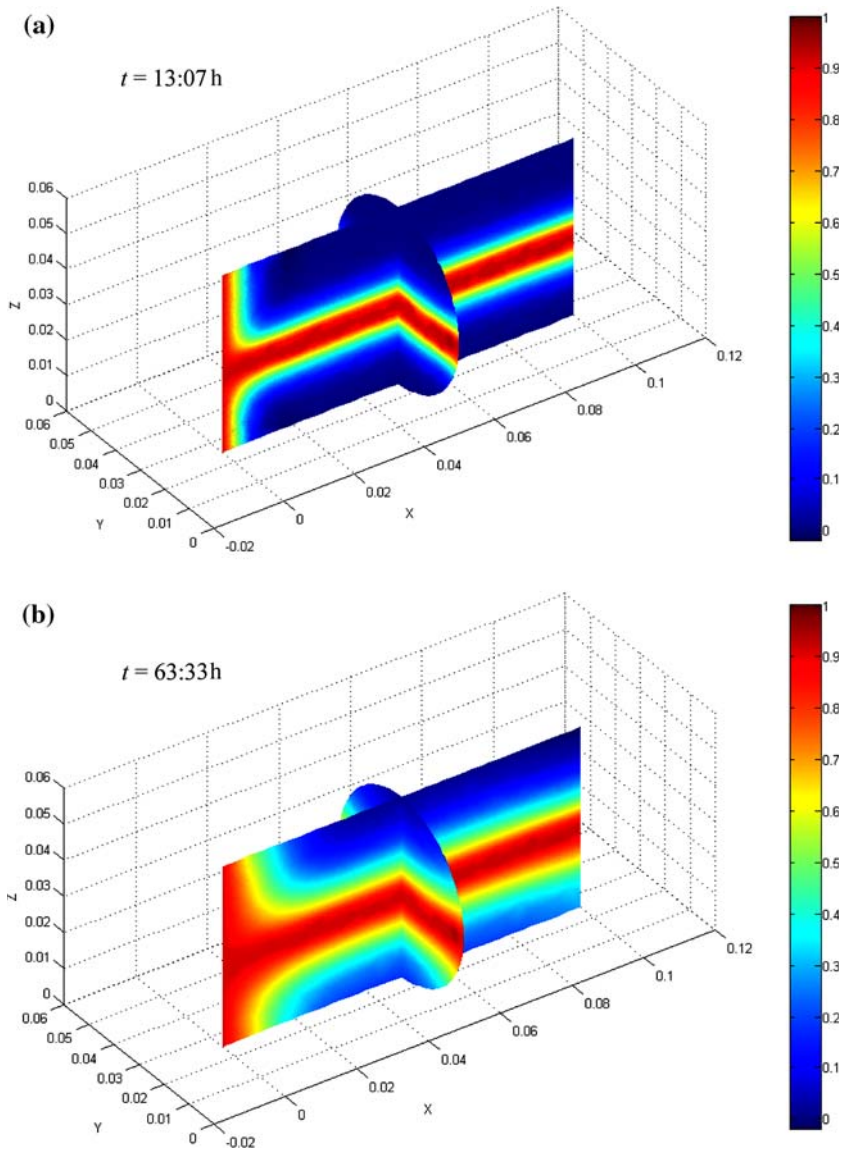


Fig. 11 Three dimensional distributions of the tracer concentration at different times, where the diffusion coefficient of rock matrix is equal to $4.0\text{e-}10\text{m}^2/\text{s}$, and the color bar indicates the relative magnitude of the tracer concentration

is not evenly distributed. The high concentration is found at the inlet side because a concentration of 1.0 is specified here. In addition, the tracer transport from inlet to outlet, as well as from fracture into surrounding rock matrix, are clearly shown.

Where convection is not suppressed within the model, distributions of the tracer concentration are shown in Fig. 12. The tracer concentration in the fracture is not equal to unity at $t = 1:38\text{h}$, which illustrates that diffusion alone cannot make the

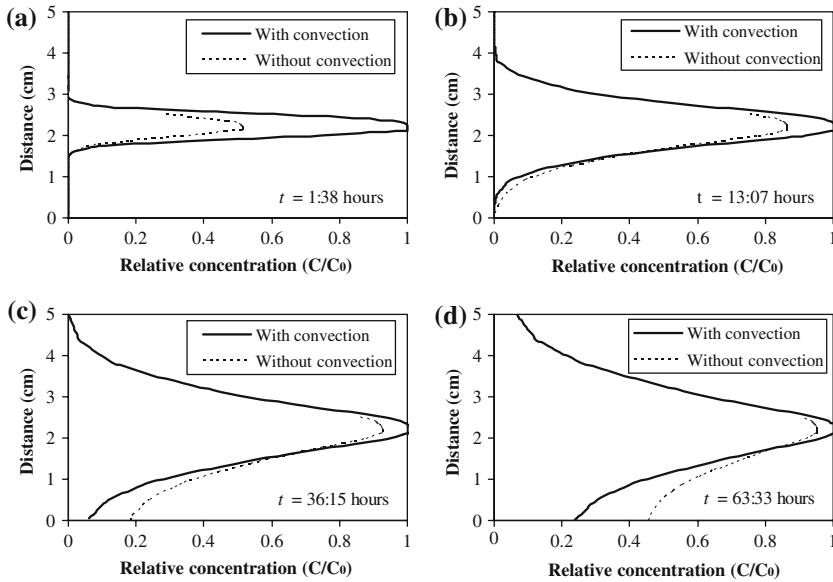


Fig. 12 Simulated distributions of the tracer concentration along the vertical diameter of the cross-section A–A with or without convection, where the diffusion coefficient of the rock matrix is equal to $4.0 \times 10^{-10} \text{ m}^2/\text{s}$

tracer fill the fracture. Even at the close of the experiment ($t = 63:33 \text{ h}$) the tracer concentration in the fracture is still less than 1.0. The effect of convection in the rock matrix is not negligible. The concentration distribution within the rock matrix also has little difference with or without convection considered. Most importantly, the effects of convection are more evident in the lower part of the rock matrix, which indicates the density has effect on transport in the rock matrix.

4 Conclusions and discussions

Integrated application of combined X-Ray CT characterization and process monitoring, with digital-image-based finite element simulations, demonstrates the importance of accommodating rock heterogeneity (porosity, hydraulic conductivity, and diffusivity) in mediating tracer transport processes in a fractured chalk. This integration leads to a digital-image-based finite element simulation tool which can be used to translate the detailed heterogeneity of the rock into phenomenological terms suitable for the characterization and analysis of flow and transport in fractured rock at meso-scales.

In this study, we treat the porosity as a function of space through use of a digital image processing technique. These property maps are ported to a finite element model capable of solving directly for the evolving fluid and tracer transport fields. The importance of discretely representing heterogeneity is demonstrated through the 3D convection-diffusion simulation of tracer transport both in the fracture and in the rock matrix. In the initial stage, the convective process has less effect on the invasion of tracer from the fracture into rock matrix, and the tracer propagates into the rock matrix predominantly through diffusion. The effect of convection in the rock matrix

is negligible in early times and it becomes apparent as the simulation progresses. As time goes to infinity, the tracer concentration should approach unity everywhere. Simulation results also show the more evident effect of convection in the lower section of the sample where density effects act to spread the slightly denser tracer solution.

Acknowledgments This work is a result of partial support under grant ARC-DP0209425 and ARC-LX0242407. This support is gratefully acknowledged. We wish to thank the Penn State Center for Quantitative imaging (CQI) where the images were taken.

References

- Blair, S.C., Cook, N.G.W.: Analysis of compressive fracture in rock statistical techniques: Part I: a non-linear rule-based model. *Int. J. Rock. Mech. Min. Sci.*, **35**, 837–848 (1998)
- Carman, P.C.: Fluid flow through granular beds. *J. Soc. Chem. Ind.*, **57**, 225 (1938)
- Chen, S., Yue, Z.Q., Tham, L.G.: Digital image-based numerical modelling method for prediction of inhomogeneous rock failure. *Int. J. Rock. Mech. Min. Sci.*, **41**, 939–957 (2004)
- Chermant, J.L.: Why automatic image analysis? An introduction to this issue. *Cement Concrete Comp.* **23**, 157–169 (2001)
- Daian, J.-F., Fernandes, C.P., Philippi, P.C., Bellini da Cunha Neto, J.A.: 3D reconstitution of porous media from image processing data using a multiscale percolation system. *J. Petrol. Sci. Eng.* **42**, 15–28 (2004)
- Diabira, I., Castanier, L.M., Kovscek, A.R.: Porosity and permeability evolution accompanying hot fluid injection into diatomite. *Petrol. Sci. Technol.*, **19**(9–10), 1167–1185 (2001)
- Finsterle, S., Fabryka-Martin, J.T., Wang, J.S.Y.: Migration of a water pulse through fractured porous media. *J. Contam. Hydrol.*, **54**, 37–57 (2002)
- Gonzalez, R.C., Woods, R.F.: *Digital Image Processing*. Addison Wesley, Reading, MA (1992)
- Hadjigeorgiou, J., Lemy, F., Cote, P., Maldague, X.: An evaluation of image analysis algorithms for constructing discontinuity trace maps. *Rock. Mech. Rock. Eng.*, **36**(2), 163–179 (2003)
- Hirono, T., Takahashi, M., Nakashima, S.: In situ visualization of fluid flow image within deformed rock by X-ray CT. *Eng. Geol.*, **70**, 37–46 (2003)
- Karacan, C.O., Mitchell, G.D.: Behavior and effect of different coal microlithotypes during gas transport for carbon dioxide sequestration into coal seams. *Int. J. Coal. Geol.*, **53**, 201–217 (2003)
- Koh, C.J., Dagenais, P.C., Larson, D.C., Murer, A.S.: Permeability damage in diatomite due to in-situ silica dissolution/precipitation. SPE 35394. In: *Proceedings of The SPE/DOE 10th Symposium on improved Oil Recovery*, Tulsa, OK, 21–24 April, (1996)
- Kozeny, J.: Sitzungsber. Akad. Wiss. Wien. Math.-Naturwiss. Kl., **136**, 271 (1927)
- Montemagno, C.D., Pyrak-Nolte, L.J.: Fracture network versus single fractures: Measurement of fracture geometry with X-ray tomography. *Phys. Chem. Earth. (A)*, **24**(7), 575–579 (1999)
- Nakashima, Y.: The use of X-ray CT to measure diffusion coefficients of heavy ions in water-saturated porous media. *Eng. Geol.*, **56**, 11–17 (2000)
- Nakashima, S.: Diffusivity of ions in pore water as a quantitative basis for rock deformation rate estimates. *Tectonophysics* **245**, 185–203 (1995)
- Nativ, R., Adar, E., Becker, A.: A monitoring network for groundwater in fractured media. *Ground Water* **37**, 38–47 (1999)
- Nguyen Q.P., Currie P.K., Zitha P.L.J.: Effect of cross-flow on foam-induced diversion in layered formations. *Soc. Petrol. Eng. J.* (2005)
- Nguyen Q.P., Currie, P.K., Zitha, P.L.J.: Determination of Foam Induced Fluid Partitioning in Porous Media using X-ray Computed Tomography, SPE 80245, SPE International Symposium on Oilfield Chemistry. Houston, TX, USA, 5–8 February (2003)
- Polak, A., Grader, A.S., Wallach, R., Nativ, R.: Tracer diffusion from a horizontal fracture into the surrounding matrix: measurement by computer tomography. *J. Contam. Hydrol.*, **67**, 95–112 (2003)
- Qi, X.Z., Zhao, J., Xiao, C.W., Liu, R.L.: A study on the quantitative processing methods of image data. In: *Proceedings of SPE International Oil and Gas Conference and Exhibition*. SPE 64626, pp. 7–11. Beijing, China (2000)

- Santos, L.O.E., Philippi, P.C., Damiani, M.C., Fernandes, C.P.: Using three-dimensional reconstructed microstructures for predicting intrinsic permeability of reservoir rocks based on a Boolean lattice gas method. *J. Petrol. Sci. Eng.*, **35**, 109–124 (2002)
- Scavia, F.R.: Determination of contact areas in rock joints by X-ray computer tomography. *Int. J. Rock. Mech. Min. Sci.*, **36**, 883–890 (1999)
- Schembre, J.M., Kovscek, A.R.: A technique for measuring two-phase relative permeability in porous media via X-ray CT measurements. *J. Petrol. Sci. Eng.*, **39**, 159–174 (2003)
- Takano, N., Zako, M., Kubo, F., Kimura, K.: Microstructure-based stress analysis and evaluation for porous ceramics by homogenization method with digital image-based modeling. *Int. J. Solids Struct.*, **40**, 1225–1242 (2003)
- Tang, C.A.: Numerical simulation of progressive rock failure and associated seismicity. *Int. J. Rock. Mech. Min. Sci.*, **34**, 249–261 (1997)
- Tang, C.A., Liu, H., Lee, P.K.K., Tsui, Y., Tham, L.G.: Numerical tests on micro–macro relationship of rock failure under uniaxial compression, part I: effect of heterogeneity. *Int. J. Rock. Mech. Min. Sci.*, **37**, 555–569 (2000)
- Tham, L.G., Li, L., Tsui, Y., Lee, P.K.K.: A replica method for observing microcracks on rock surface. *Int. J. Rock. Mech. Min. Sci.*, **40**, 785–794 (2003)
- Tidwell, V.C., Meigs, L.C., Christian-Frear, T., Boney, C.M.: Effects of spatially heterogeneity porosity on matrix diffusion as investigated by X-ray absorption imaging. *J. Contam Hydrol.*, **42**, 285–302 (2000)
- Vinegar, H.J., Wellington, S.L.: Tomographic imaging of three-phase flow experiments. *Rev. Sci. Inst.*, 96–107 (1987)
- Vukoturi, V.S., Lama, R.D., Saluja, S.S.: Handbook on Mechanics Properties of Rocks, vol. 1. Trans. Tech. Publications, Switzerland (1974)
- Wildenschild, D., Hopmans J.W., Vaz, C.M.P., Rivers, M.L., Rikard, D., Christensen, B.S.B.: Using X-ray computed tomography in hydrology: systems resolutions and limitations. *J. Hydrol.*, **267**, 285–297 (2002)
- Withjack, E.M., Durham, J.R.: Characterization and saturation determination of reservoir meta-graywacke from the Geysers corehole SB-15-D (USA), using nuclear magnetic resonance spectrometry and X-ray computed tomography. *Geothermics* **30**, 255–268 (2001)
- Yue, Z.Q., Chen, S., Tham, L.G.: Finite element modeling of geomaterials using digital image processing. *Comput. Geotech.*, **30**, 375–397 (2003)
- Zhu, W.C., Tang, C.A.: Micromechanical model for simulating the fracture process of rock. *Rock Mech. Rock. Eng.*, **37**(1), 25–56 (2004)
- Zitha, P.L.J., Nguyen Q.P., Currie, P.K.: Effect of Flow Velocity and Rock Layering on Foam Flow: an X-ray Computed Tomography Study, SPE 80530, SPE Asia Pacific Oil and Gas Conference and Exhibition held in Jakarta, Indonesia, 15–17 April (2003)